Journal of Alloys and Compounds 586 (2014) 656–662

Contents lists available at ScienceDirect

Journal of Alloys and Compounds

journal homepage: www.elsevier.com/locate/jalcom

Electronic structures of long periodic stacking order structures in Mg: A first-principles study

William Yi Wang [a,b,*], Shun Li Shang [a], Yi Wang [a], Kristopher A. Darling [b], Laszlo J. Kecskes [c], Suveen N. Mathaudhu [d], Xi Dong Hui [b], Zi-Kui Liu [a,*]

[a] Department of Materials Science and Engineering, The Pennsylvania State University, University Park, PA 16802, USA
[b] State Key Laboratory for Advanced Metals and Materials, University of Science and Technology Beijing, Beijing 100083, China
[c] U.S. Army Research Laboratory, Weapons and Materials Research Directorate, RDRL-WMM-B, Aberdeen Proving Ground, MD 21005, USA
[d] Materials Science Division, U.S. Army Research Office, Research Triangle Park, NC 27709, USA

ARTICLE INFO

Article history:
Received 20 August 2013
Received in revised form 8 October 2013
Accepted 9 October 2013
Available online 26 October 2013

Keywords:
Mg alloys
Stacking faults
Long period stacking order (LPSO)
Deformation electron density

ABSTRACT

Long period stacking order (LPSO) structures, such as 6H, 10H, 14H, 18R and 24R, play significant roles in enhancing the mechanical properties of Mg alloys and have been largely investigated separately. In the present work, through detailed investigations of deformation electron density, we show that the electron structures of 10H, 14H, 18R and 24R LPSO structures in Mg originate from those of deformation stacking faults in Mg, and their formation energies can be scaled with respect to formation energy and the number of layers of deformation stacking faults, while the electron structure and formation energy of the 6H LPSO structure are between those of deformation and growth stacking faults. The simulated images of high resolution transmission electron microscopy compare well with experimental observed ones. The understanding of LPSO structures in Mg enables future quantitative investigations of effects of alloying elements on properties of LPSO structures and Mg alloys.

1. Introduction

As the lightest metallic structural materials, Mg alloys are particularly attractive for transportation applications such as automobiles and aircrafts for weight reducing and higher fuel efficiency [1]. Numerous efforts have been made in order to increase the strength and the ductility of Mg alloys. In recent years, Mg-RE alloys with excellent mechanical properties have been obtained for combining fine grain size, precipitates, and long period stacking order (LPSO) structures. For instance, the tensile yield strength and the elongation of $Mg_{97}Y_2Zn_1$ (at.%) alloy with the 6H LPSO structure produced by rapid solidification can reach 610 MPa and 5%, respectively, with grain sizes in range of 100 nm–150 nm [2]. When the grain size of Mg matrix is about 330 nm, the tensile yield strength and the elongation become 400 MPa and 2%, respectively [3]. It is commonly accepted that fine precipitates or local clustering of solute atoms together with different types of LPSO structures, including 6H, 10H, 14H, 18R and 24R, contribute to strengthening of Mg alloys [4–13].

The 6H, 10H, 14H, 18R and 24R LPSO structures have been reported in Mg alloys by atomic-resolution Z-contrast scanning transmission electron microscopy (STEM) [2,4,12,14–16] and are typically characterized by their stacking sequence of close packed planes as listed in Table 1. It has been estimated that the formation energy of 6H twice that of the growth fault (I1), while the formation energies of other LPSO structures depend on the number of the deformation fault (I2) they contain [17]. The ABCA-type stacking sequence in I2, 14H and 18R are similar, but with distinct spatial arrangements [16,18]. This similarity has in some cases led to transformations between variant structure, such as 18R to 14H observed at high temperature by transmission electron microscopy (TEM) in a Mg–2Zn–8Y–0.6Zr (wt%) alloy [16]. Such intricate connections among stacking faults and all LPSO structure have not been fully explored and understood, particularly the electronic structures of various LPSO structures and their dependences on alloying elements. Experimentally, the technique of electron tomography provides not only the atomic structure, but also the electronic structures together with simulations based on density functional theory (DFT) [19], such as the nature of chemical bond and the charge redistribution [20–25]. It is noted that the electron density predicted from DFT-based first-principles calculations can be directly compared with the charge transfer obtained from electron tomography measurements and used to simulate the HRTEM images by projecting the electron density or converting the electron density into electron scattering factor [25–28].

* Corresponding authors. Address: Department of Materials Science and Engineering, The Pennsylvania State University, University Park, PA 16802, USA. Tel.: +1 814 8651934, fax: +1 707 8851934 (Z.-K. Liu), tel.: +1 814 863 9957 (W.Y. Wang).
E-mail addresses: yuw129@psu.edu (W.Y. Wang), dr.liu@psu.edu (Z.-K. Liu).

0925-8388/$ - see front matter © 2013 Elsevier B.V. All rights reserved.
http://dx.doi.org/10.1016/j.jallcom.2013.10.068

Table 1
Stacking sequence, lattice parameter (a), bulk modulus (B_0) and formation energy (γ) of stacking faults and LPSO structures in Mg. B_0 and a (with c/a = 1.621) are obtained through four parameters Birch–Murnaghan equation of states.

	Stacking order	Lattice parameter		B_0 (GPa)	γ_{mJ/m^2}	$\frac{\gamma}{\gamma_{I2}}$
		a (Å)	C-LPSOÅ			
Mg	$\cdots ABAB\cdots$ or $\cdots BCBC\cdots$ or $\cdots ACAC\cdots$	3.195 3.189[a] 3.215[b] 3.199[j]	–	35.9 35.6[c] 36.9[d]	–	–
I1	$\cdots CBCBC\dot{B}ABABAB\cdots$	3.196	–	35.6	14.4 18.0[h]	0.3
I2	$\cdots ABABA\dot{B}\dot{C}ACACAC\cdots$	3.198	–	35.2	48.2 33.8[h] 45.0[i]	1
6H	$\dot{A}BAB\dot{A}C$ or $\dot{B}CBC\dot{B}A$	3.197 3.22[e] 3.202[g] 3.200[j]	15.549 15.6[e] 15.482[g]	35.6–36.28[g]	44.644.1[h]	0.9I2 2I1[h]
10H	$\dot{C}BCB\dot{C}\dot{A}BAB\dot{A}$	3.198 3.25[f]3.202[j]	25.917 26.03[f]	35.5	98.2 65.0[h]	2.0 2[h]
14H	$\dot{A}BABAB\dot{A}\dot{C}BCBCB\dot{C}$	3.197 3.25[f]3.199[j]	36.273 36.94[f]	34.5	93.2 63.3[h]	1.9 2[h]
18R	$\dot{A}CBCBC\dot{B}\dot{A}CACA\dot{C}\dot{B}ABA\dot{B}$	3.197 3.20[f] 3.202[j]	46.644 46.78[f]	35.6	163.4 94.0[h]	3.4 3[h]
24R	$\dot{A}BABABA\dot{B}\dot{C}ACACAC\dot{A}\dot{B}CBCBCB\dot{C}$	3.197 3.22[f]	62.185 61.81[f]	33.6	164.1 101.6[h]	3.4 3[h]

Note: The letter with a dot above is applied to identify the fault layer.
[a] Wang et al., first-principles calculations with PAW-GGA [49].
[b] Karen et al., powder neutron diffraction measurement (c/a = 1.623) [50].
[c] Wazzan et al., experimental measurements of single crystal Mg [51].
[d] Slutsky et al., experimental measurements of single crystal Mg [52].
[e] Inoue et al., high temperature extrusion prepared $Mg_{97}Zn_1Y_2$ (at.%) observed by HRTEM [2].
[f] Matsuda et al., rapidly solidified $Mg_{97}Zn_1Y_2$ (at.%) alloys observed by HRTEM [14].
[g] Tang et al., first-principles calculations of with PAW-GGA (c/a = 1.612) [53].
[h] Fan et al., first-principles calculations with PAW-GGA [17].
[i] Pan et al., first-principles calculations with PAW-GGA [18].
[j] Iikubo et al., first-principles calculations with PAW-GGA (c/a = 1.624) [54].

Recently, the authors used electron localization morphologies of growth (I1), deformation (I2), and extrinsic faults of hcp Mg to provide quantitative descriptions of charge transfer between atoms in and out of the stacking faults and physical interpretations of the relation between stacking fault energy and deformation charge density [29]. It was shown that the stacking fault energy ascends in the order of I1, I2, and extrinsic faults and is proportional to the square of the difference of maximum deformation charge density, the difference of maximum electron localization function, and the number of faulted layers. In the present work, the electron localization morphologies of LPSO structures in hcp Mg are investigated in details to unearth the intrinsic correlations among various LPSO structures. Such knowledge paves the path to understand the effects of alloying elements on properties of LPSO structures and design Mg alloys for better performance.

2. Methodology

In the present first-principles calculations, the orthorhombic supercell sizes of 6H, 10H, 14H, 18R and 24R LPSO structures are $2a \times 4\sqrt{3}a \times 3c$, $a \times \sqrt{3}a \times 5c$, $a \times \sqrt{3}a \times 7c$, $a \times \sqrt{3}a \times 9c$ and $a \times \sqrt{3}a \times 12c$ with 96, 20, 28, 36 and 48 atoms, respectively, where a and c are the theoretical lattice parameters of primitive hcp Mg and an orientation relationship of $\langle 01\bar{1}0\rangle_{hcp}||\langle 100\rangle_{s.c.}$, $\langle 1\bar{2}10\rangle_{hcp}||\langle 010\rangle_{s.c.}$ and $\langle 0001\rangle_{hcp}||\langle 001\rangle_{s.c.}$. Setting parameters for I1 and I2 can be found in our previous work [29].

Calculations of electronic structures and formation energies at 0 K are carried out by means of the Vienna ab initio simulation package [30,31] with the generalized gradient approximation [32] for the exchange-correction functional and the projector augmented wave [33] for the electron–ion interaction. The wave functions are sampled on Γ-centered Monkhorst–Pack grids of $9 \times 3 \times 4$, $19 \times 11 \times 2$, $19 \times 11 \times 2$, $19 \times 11 \times 1$, $19 \times 11 \times 1$ for 6H, 10H, 14H, 18R and 24R structures generated automatically with same scaling length (l = 60), respectively. The plane wave cutoff energy is set as 300 eV, i.e. 1.4 times the default cutoff energy for high accuracy calculations [34], and the energy convergence criterion of electronic self-consistency is 10^{-6} eV/atom. While the structures are fully relaxed by the Methfessel–Paxton technique [35], the final total energy calculations are performed by the tetrahedron method incorporating Blöchl correction [36].

Four-parameter Birch–Murnaghan equation of states [37–39] is used to describe the relation between energy and volume as follows,

$$E(V) = a + \frac{B_0 V}{B_0'}\left(1 + \frac{(V_0/V)^{B_0'}}{B_0' - 1}\right) \quad (1)$$

where the fitting parameter $a = E_0 - \frac{B_0 V}{B_0' - 1}$. The parameters V_0, E_0, B_0 and B_0' represent the equilibrium volume, energy, bulk modulus and its first derivative with respect to pressure, respectively. The formation energy of LPSO structures, γ, can be obtained through

$$\gamma = \frac{1}{A}(E_{LPSO} - E_{Bulk}) \quad (2)$$

where E_{LPSO} and E_{Bulk} are the total energies of supercells with and without LPSO structures, respectively, and A is the area of basal plane of supercells.

Deformation electron density ($\Delta\rho$) [40,41] is used to characterize the electronic structures of LPSO structures. It is calculated through the charge density difference between the fully relaxed structure of self-consistent calculations and the same structure of non self-consistent calculations. The isosurface structures with different values of $\Delta\rho$ are generated using VESTA [42,43]. In the literature HRTEM images are analyzed on the independent atom model (IAM) [25,40] or the procrystal model [24] or the electron density from DFT with a correction in term of charge density difference [27]. It has been shown that the intensity difference between electron densities from DFT and IAM is sensitive to the structure defect and the impurity (even lightweight element) [25]. The simulated HRTEM images in this work are obtained through the projection of the calculated deformation charge density ($\Delta\rho$) using the procedure described in Ref. [25].

3. Results and discussions

Table 1 summarizes the predicted stacking sequence, lattice parameter (a and c), bulk modulus (B_0), formation energy (γ) of I1, I2, and LPSO structures, and the ratio of formation energy with respect to that of I2 (γ/γ_{I2}). The total energies of I1, I2, and LPSO structures as a function of volume are fitted by a four parameters Birch-Murnaghan equation of state (shown in Fig. S1 in the supplemental information). It can be seen in Table 1 that our predicted lattice parameters of I1, I2 and LPSO structures are consistent with experimental data, while bulk modules are lower than that of Mg indicating the increase of atomic volume cased by fault layers and matching well with our previous prediction (the B_0 of FCC Mg decreases from 35.7 of HCP to 34.7 GPa with the volume increases from 22.887 of HCP to 23.068 Å^3/atom) [39]. The ratios of formation energy indicate that the formation energies of LPSO structures in Mg can be scaled to the formation energy of I2, approximately one for 6H, two for 10H and 14H, and three for 18R and 24R, respectively.

To understand this scaling correlation, Fig. 1 plots the isosurface of the maximum deformation electron density ($-\Delta\rho_{max}$) for I1, I2 and LPSO structures in the prismatic plane of $\{11\bar{2}0\}_{hcp}||\{100\}_{s.c.}$, using the positive and negative mode in VESTA [42,43]. Since the charge density is a scalar field, the change in electron distribution results in directional bonds [44] and can be correlated to the formation energy of stacking faults [45] and LPSO structures. Furthermore, the examination of deformation electron density can directly reveal the fault layers and its number in those structures through isosurface structure of each layer [29]. It can be seen in Fig. 1 that two fault layers in 6H LPSO with altered charge density are separated by one non-fault plane, different from both I1 with single fault layers separated by three non-fault layers and I2 with double-fault layers separated by three and five non-fault layers, respectively. That is the reason why the predicted γ_{6H} is larger than $2\gamma_{I1}$ and closer to, but smaller than γ_{I2}, indicating stronger interactions of two fault layers when they become closer in accordance with previous theoretical work [46]. It is further observed in Fig. 1 that all the 10H, 14H, 18R and 24R structures have double-fault layers like I2, and the numbers of non-fault layers between double-fault layers are three, five, four, and six, respectively, equal or larger than that in I2. The total numbers of double-fault layers are two for 10H and 14H structures and three for 18R and 24R structures, respectively, coinciding with the ratios of their formation energies to that of I2 as discussed above. The stacking sequences across the fault layers are highlighted by rectangles with 3 or 4 atomic layers of $A\dot{B}C$ or $A\dot{B}\dot{C}A$ and solid and dotted lines for different directions, further demonstrating the correlations between I1 and 6H, and I2 and other LPSO structures.

Fig. 2 presents the $0.5\Delta\rho_{max}$ isosurface in stacking faults and LPSO structures in the prismatic plane. At this level, variation of the chemical bond structure from non-fault layer to fault layer is revealed clearly. It is observed that all LPSO structures have similar bond morphologies as I1 and I2 stacking faults [29,47], i.e.

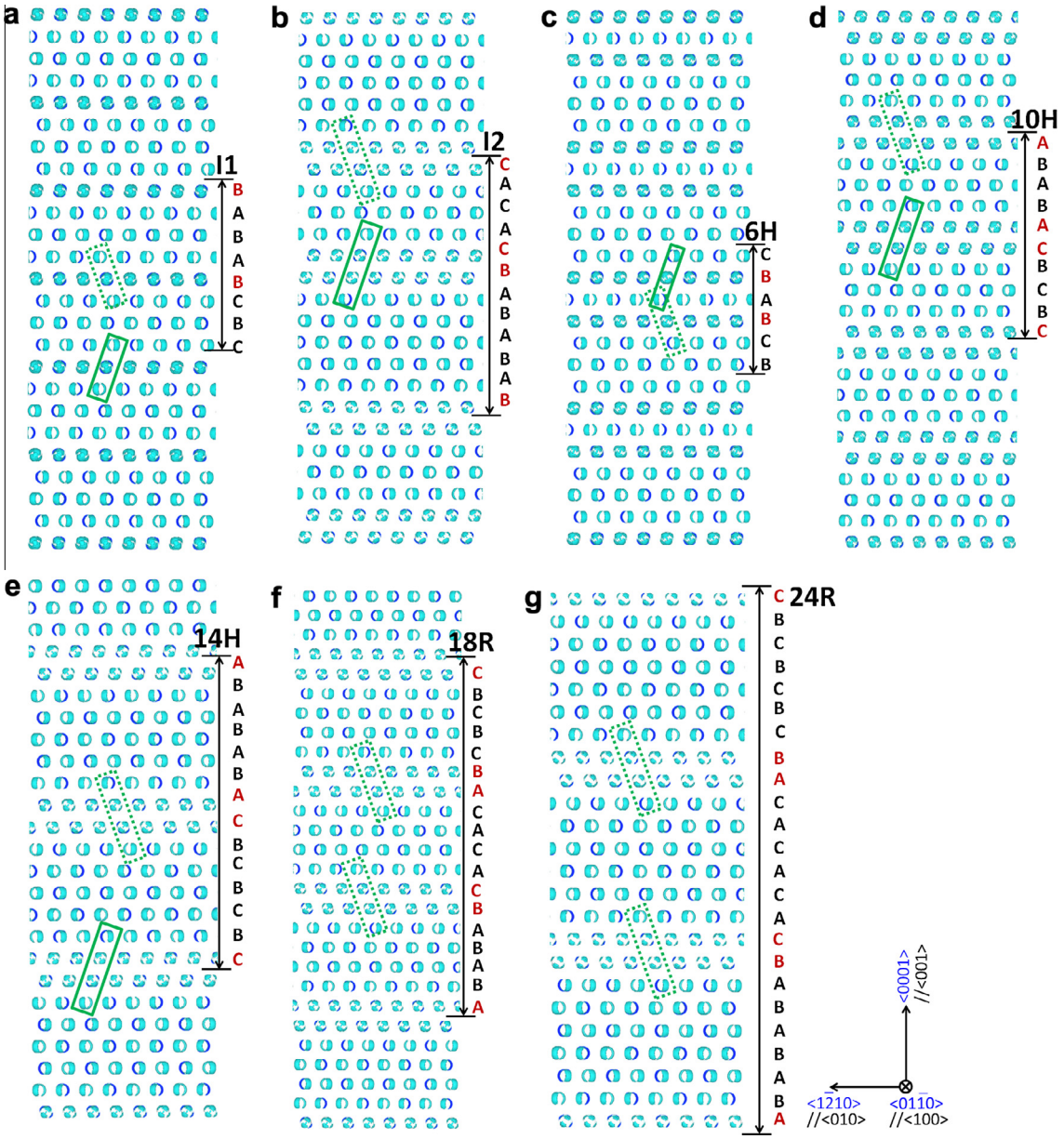

Fig. 1. $(100)_{s.c.}$ Plane view of isosurface of deformation charge density, $\Delta\rho = -\Delta\rho_{max}$, a–g:I1, I2, 6H, 10H, 14H, 18R and 24R, generated using VESTA [42,43], with letters in red denoting fault layers and rectangles denoting atomic layers across fault layers. (For interpretation of the references to colour in this figure legend, the reader is referred to the web version of this article.)

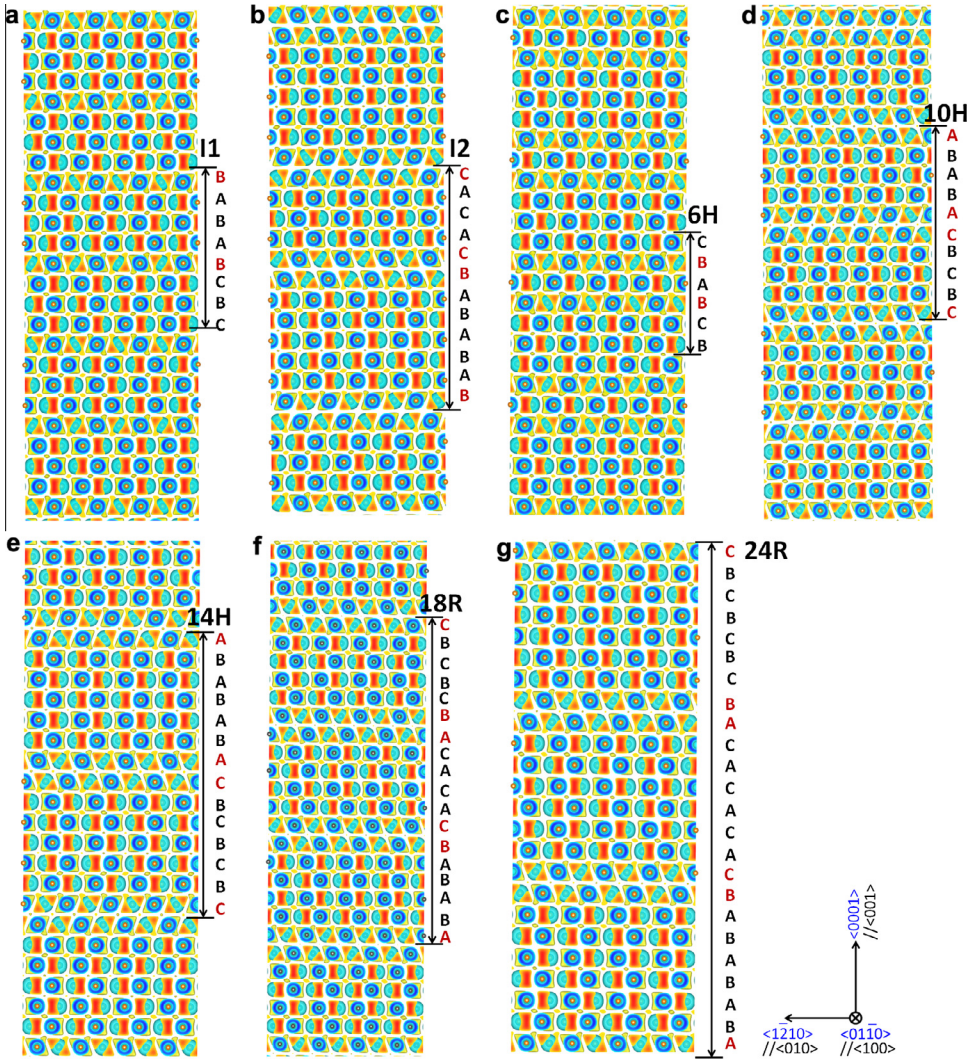

Fig. 2. $0.5\Delta\rho_{max}$ isosurface of (1 0 0) plane view, a–g: I1, I2, 6H, 10H, 14H, 18R and 24R, generated using VESTA [42,43], with letters in red denoting fault layers.

rod-shaped in non-fault layers and tetrahedron-shaped in fault layers, respectively. It should be noted that the tetrahedron-shaped directional bonds are characteristics of the fcc structure such as Al [40], in line with the fact that stacking faults and LPSO structures represent the local fcc atomic environment in a hcp matrix. Based on the information presented in Figs. 1 and 2, it seems logical to correlate the formation energy of LPSO structures with the number of fault or double-fault layers, shown in Fig. 3 with a near linear relation depicted. This indicates the weak interaction between double-fault layers in the LPSO structures.

Fig. 4 shows the simulated (1 0 0) HRTEM images of growth fault and deformation fault using the technique described in the Method section of this paper. Fault and non-fault layers are labeled in red and blue letters, respectively. The stacking sequences of I1 and I2 can be wrote as $A\dot{B}C$ and $A\dot{B}\dot{C}A$ across the fault layers, forming basic unites of rectangles with 3 and 4 atomic layers, respectively, as the same as those shown in Fig. 1a and b, which have been used to describe the TEM images of 14H and 18R LPSO structures in Mg alloys [16]. It is to be noted that the effects of alloying elements on LPSO structures will be discussed in a paper under preparation.

Fig. 5 shows the simulated (pure Mg) and experimental ($Mg_{97}Zn_1Y_2$) (1 0 0) TEM images of 6H and 10H structures. It can be seen in Fig. 5a that the non-fault layer between the two-fault layers in 6H is a mirror plane with the stacking sequence of three

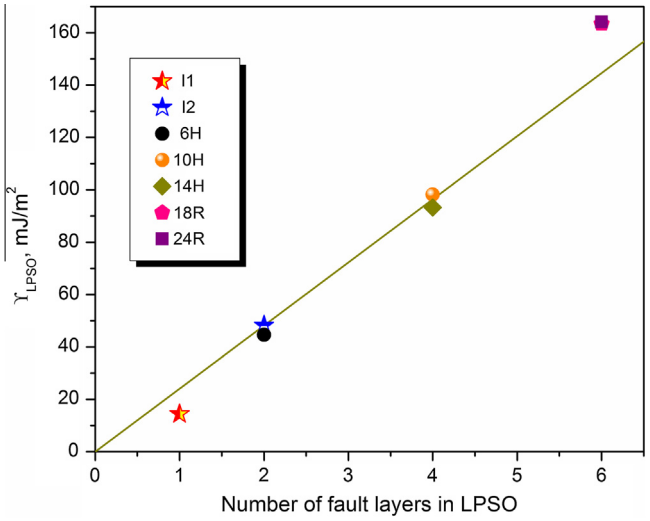

Fig. 3. Correlation between the formation energy of LPSO structures and the number of fault layers. The line represents the ideal linear relation between the formation energy and the number of fault layers.

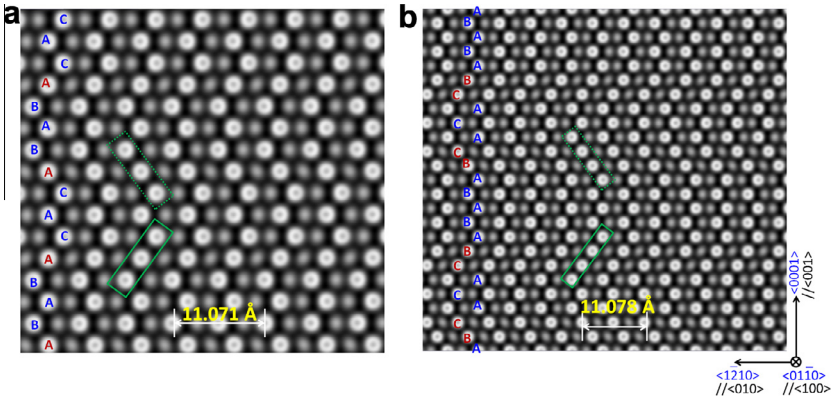

Fig. 4. Simulated (100) HRTEM images of the stacking faults in I1 (a) and I2 (b). Fault and non-fault layer are labeled with letters in red and blue, respectively. Stacking features across fault and non-fault layers are highlighted by rectangle and triangle, respectively. (For interpretation of the references to colour in this figure legend, the reader is referred to the web version of this article.)

atomic layers of $A\dot{B}C$ to both sides of the mirror plane, similar to that in I1. While in 10H shown in Fig. 5b, the non-fault layer between two non-fault layers is a mirror plane with the stacking sequence of four atomic layers of $A\dot{B}\dot{C}A$ to both sides of the mirror plane, similar to that in I2. On the contrary, there are no mirror planes in 14H, 18R and 24H though the stacking sequence of four atomic layers of $A\dot{B}\dot{C}A$, similar to that in I2, seems sheared in opposite directions in 14H and in the same direction in 18R and 24H, as shown in Fig. 6. The observation in 14H is consistent with interpretation of the two twin-related building blocks with ABCA-type stacking sequence derived from TEM results [48]. It should be emphasized that the electron localization morphology in this work clearly reveals that each twin-related building block is made up of two fault layers, i.e. $A\dot{B}\dot{C}A$ shown in Fig. 6a.

The detailed electronic structures of LPSO structures discussed above provide insights on transformations between them. It is shown that the densities of fault layers are in the descending order from 10H, 18R, 14H, to 24R as 2/5, 1/3, 2/7, and 1/4. The transformation from LPSO structures with a higher density of fault layers to those with lower density is thus energetically favorable such as the 18R to 14H transformation observed experimentally at high temperatures [16]. Since the formation of fault layers is related to the dissociation of dislocations to Shockley partials, the above transformation thus reduces the dislocation density during heat

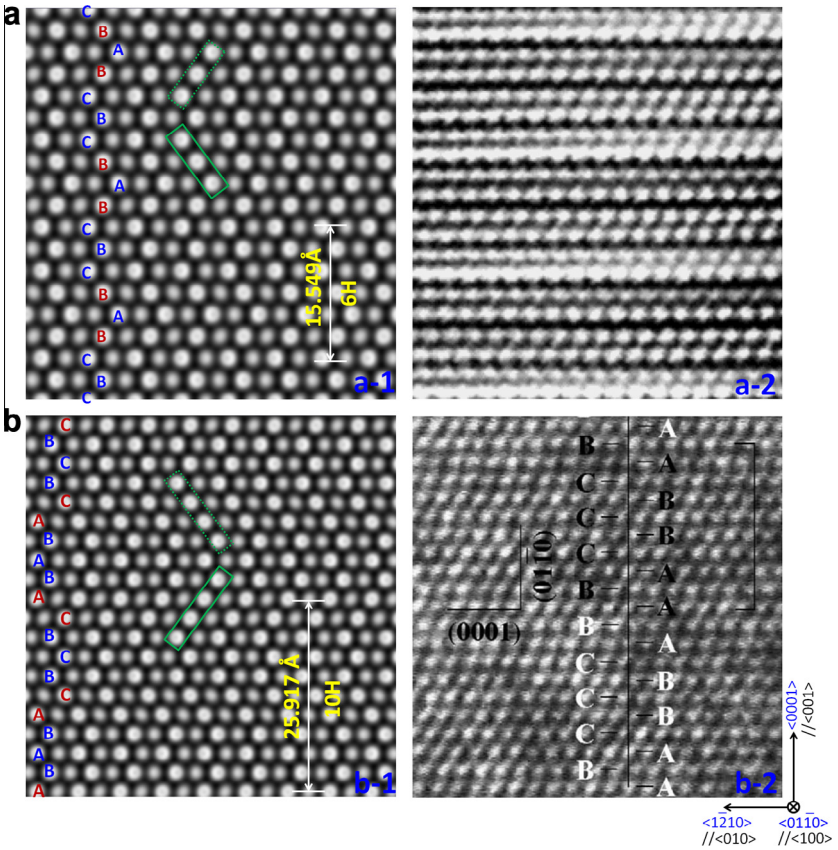

Fig. 5. Simulated (100) HRTEM images in 6H (a) and 10H (b) with the stacking sequence of four atomic layers highlighted by the rectangles and fault layers in red. The HRTEM images of 6H and 10H of $Mg_{97}Zn_1Y_2$ in a-2 and b-2 are reproduced from [2] and [14] with permissions of The Japan Institute of Metals and by Elsevier, respectively. (For interpretation of the references to colour in this figure legend, the reader is referred to the web version of this article.)

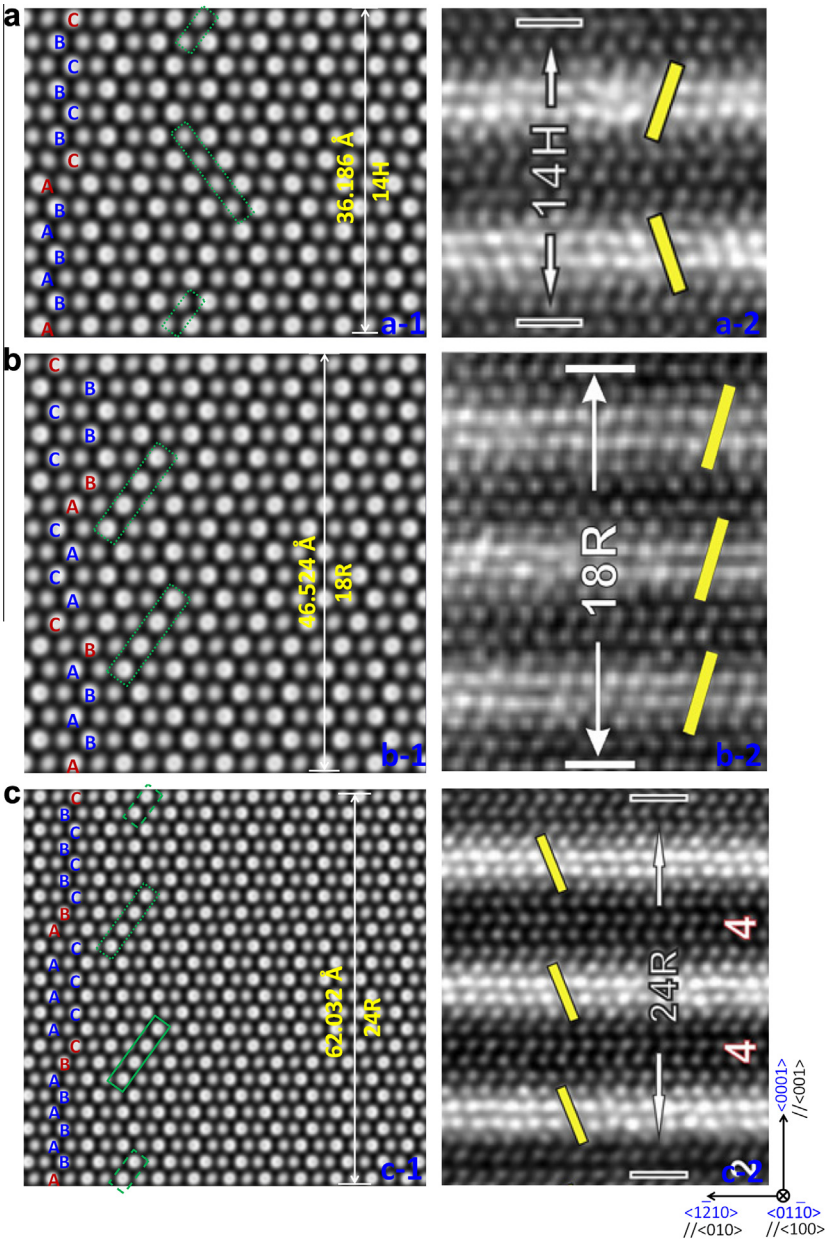

Fig. 6. Simulated (1 0 0) HRTEM images with stacking sequence of four atomic layers in 14H (a), 18R (b) and 24H (c) structures and fault layers in red. The STEM images of 14H, 18R and 24R of Mg–Zn–Y alloys in a-2, b-2 and c-2 are reproduced from [16] with permissions by Elsevier. (For interpretation of the references to colour in this figure legend, the reader is referred to the web version of this article.)

treatment. It should be pointed out that the higher density of fault layers does not mean higher formation energy of LPSO structures shown in Table 1 and Fig. 3, which are correlated with the total number of fault layers in each LPSO structure.

4. Conclusions

In summary the electronic structures of 6H, 10H, 14H, 18R and 24R LPSO structures are investigate by means of first-principles calculations and are observed to be similar to that of deformation stacking fault. Except 6H, all of them can be considered as stacking of double-fault layers with variable non-fault layers between. The electron localization morphology further confirms the fcc characteristics of the fault layers based on the tetrahedron-shaped directional bonds. The simulated HRTEM images reveal a mirror plane with the stacking sequence of three atomic layers in 6H and four atomic layers in 10 H, and a sheared displacement of the stacking sequence of four atomic layers in 14H, 18R and 24R. It is articulated that transformation between LPSO structures is related to the reduction of dislocation density during heat treatment.

Acknowledgments

This work was financially supported by the U.S. Army Research Lab (Project No. W911NF-08-2-0064) and the National Science Foundation (Grant No. DMR-1006557) in the United States, National Natural Science Foundation of China (Grant No. 51071018). W.Y. Wang acknowledges the support from the Project Based Personnel Exchange Program with China Scholarship Council and American Academic Exchange Service ([2008] 3072). First-principles calculations were carried out on the LION clusters supported by the Materials Simulation Center and the Research Computing

and Cyberinfrastructure unit at the Pennsylvania State University. Calculations were also carried out on the CyberStar cluster funded by NSF through Grant OCI-0821527, and partially on resources of the National Supercomputer Center in Shenzhen.

Appendix A. Supplementary material

Supplementary data associated with this article can be found, in the online version, at http://dx.doi.org/10.1016/j.jallcom.2013.10.068.

References

[1] T.M. Pollock, Science 328 (2010) 986–987.
[2] A. Inoue, M. Matsushita, Y. Kawamura, K. Amiya, K. Hayashi, J. Koike, Mater. Trans. 43 (2002) 580–584.
[3] B. Chen, D.L. Lin, X.Q. Zeng, C. Lu, J. Alloys Comp. 440 (2007) 94–100.
[4] Y. Kawamura, M. Yamasaki, Mater. Trans. 48 (2007) 2986–2992.
[5] E. Onorbe, G. Garces, P. Perez, P. Adeva, J. Mater. Sci. 47 (2012) 1085–1093.
[6] M. Yamasaki, K. Hashimoto, K. Hagihara, Y. Kawamura, Acta Mater. 59 (2011) 3646–3658.
[7] J.F. Nie, Metall. Mater. Trans. A 43 (2012) 3891–3939.
[8] D. Egusa, E. Abe, Acta Mater. 60 (2012) 166–178.
[9] Z. Leng, J.H. Zhang, M.L. Zhang, X.H. Liu, H.B. Zhan, R.Z. Wu, Mater. Sci. Eng. A 540 (2012) 38–45.
[10] M. Yamasaki, T. Anan, S. Yoshimoto, Y. Kawamura, Scr. Mater. 53 (2005) 799–803.
[11] T. Itoi, T. Seimiya, Y. Kawamura, M. Hirohashi, Scr. Mater. 51 (2004) 107–111.
[12] E. Abe, Y. Kawamura, K. Hayashi, A. Inoue, Acta Mater. 50 (2002) 3845–3857.
[13] W.W. Jian, G.M. Cheng, W.Z. Xu, H. Yuan, M.H. Tsai, Q.D. Wang, C.C. Koch, Y.T. Zhu, S.N. Mathaudhu, Mater. Res. Lett. 1 (2013) 61–66.
[14] M. Matsuda, S. Ii, Y. Kawamura, Y. Ikuhara, M. Nishida, Mater. Sci. Eng. A 393 (2005) 269–274.
[15] J.S. Zhang, C.J. Chen, Z.P. Que, W.L. Cheng, J.D. Xu, J.J. Kang, Mater. Sci. Eng. A 552 (2012) 81–88.
[16] Y.M. Zhu, A.J. Morton, J.F. Nie, Acta Mater. 60 (2012) 6562–6572.
[17] T.W. Fan, B.Y. Tang, L.M. Peng, W.J. Ding, Scr. Mater. 64 (2011) 942–945.
[18] F.S. Pan, S.Q. Luo, A.T. Tang, J. Peng, Y. Lu, Prog. Nat. Sci. 21 (2011) 485–490.
[19] W. Kohn, L. Sham, Phys. Rev. 140 (1965) 1133–1138.
[20] I. Arslan, E.A. Stach, Nat. Mater. 11 (2012) 908–909.
[21] S. Van Aert, K.J. Batenburg, M.D. Rossell, R. Erni, G. Van Tendeloo, Nature 470 (2011) 374–377.
[22] D. Van Dyck, F.R. Chen, Nature 486 (2012) 243–246.
[23] S.-O. Guillaume, B. Zheng, J.-C. Charlier, L. Henrard, Phys. Rev. B 85 (2012) 035444.
[24] L. Wu, Y. Zhu, T. Vogt, H. Su, J.W. Davenport, J. Tafto, Phys. Rev. B 69 (2004) 064501.
[25] J.C. Meyer, S. Kurasch, H.J. Park, V. Skakalova, D. Kunzel, A. Gross, A. Chuvilin, G. Algara-Siller, S. Roth, T. Iwasaki, U. Starke, J.H. Smet, U. Kaiser, Nat. Mater. 10 (2011) 209–215.
[26] N. Shibata, S.D. Findlay, S. Azuma, T. Mizoguchi, T. Yamamoto, Y. Ikuhara, Nat. Mater. 8 (2009) 654–658.
[27] S. Mogck, B.J. Kooi, J.T.M. De Hosson, M.W. Finnis, Phys. Rev. B 70 (2004) 245427.
[28] T. Gemming, G. Mobus, M. Exner, F. Ernst, M. Ruhle, J. Microsc.-Oxf. 190 (1998) 89–98.
[29] W.Y. Wang, S.L. Shang, Y. Wang, K.A. Darling, S.N. Mathaudhu, X.D. Hui, Z.K. Liu, Chem. Phys. Lett. 551 (2012) 121–125.
[30] G. Kresse, J. Furthmuller, Phys. Rev. B 54 (1996) 11169–11186.
[31] G. Kresse, J. Furthmuller, Comput. Mater. Sci. 6 (1996) 15–50.
[32] G. Kresse, D. Joubert, Phys. Rev. B 59 (1999) 1758–1775.
[33] Y. Wang, J.P. Perdew, Phys. Rev. B 44 (1991) 13298–13307.
[34] Y. Wang, L.Q. Chen, Z.K. Liu, S.N. Mathaudhu, Scr. Mater. 62 (2010) 646–649.
[35] M. Methfessel, A.T. Paxton, Phys. Rev. B 40 (1989) 3616–3621.
[36] P.E. Blochl, O. Jepsen, O.K. Andersen, Phys. Rev. B 49 (1994) 16223–16233.
[37] F. Birch, Phys. Rev. 71 (1947) 809.
[38] F. Birch, J. Geophys. Res. 83 (1978) 1257–1268.
[39] S.L. Shang, A. Saengdeejing, Z.G. Mei, D.E. Kim, H. Zhang, S. Ganeshan, Y. Wang, Z.K. Liu, Comput. Mater. Sci. 48 (2010) 813–826.
[40] P.N.H. Nakashima, A.E. Smith, J. Etheridge, B.C. Muddle, Science 331 (2011) 1583–1586.
[41] P.A. Midgley, Science 331 (2011) 1528–1529.
[42] K. Momma, F. Izumi, J. Appl. Crystallogr. 41 (2008) 653–658.
[43] K. Momma, F. Izumi, J. Appl. Crystallogr. 44 (2011) 1272–1276.
[44] S. Ogata, J. Li, S. Yip, Science 298 (2002) 807–811.
[45] Y. Qi, R.K. Mishra, Phys. Rev. B 75 (2007). 224105.
[46] T.W. Fan, Q. Zhang, B.Y. Tang, L.M. Peng, W.J. Ding, Eur. phys. J. B 82 (2011) 143–146.
[47] P. Blaha, K. Schwarz, P.H. Dederichs, Phys. Rev. B 38 (1988) 9368–9374.
[48] Y.M. Zhu, A.J. Morton, J.F. Nie, Acta Mater. 58 (2010) 2936–2947.
[49] Y. Wang, S. Curtarolo, C. Jiang, R. Arroyave, T. Wang, G. Ceder, L.Q. Chen, Z.K. Liu, CALPHAD 28 (2004) 79–90.
[50] P. Karen, A. Kjekshus, Q. Huang, V.L. Karen, J. Alloys Comp. 282 (1999) 72–75.
[51] A.R. Wazzan, L.B. Robinson, Phys. Rev. 155 (1967) 586–594.
[52] L.J. Slutsky, C.W. Garland, Phys. Rev. 107 (1957) 972–976.
[53] P.Y. Tang, B.Y. Tang, L.M. Peng, W.J. Ding, Mater. Chem. Phys. 131 (2012) 634–641.
[54] S. Iikubo, K. Matsuda, H. Ohtani, Phys. Rev. B 86 (2012) 054105.